NANO LETTERS

pubs.acs.org/NanoLett

Letter

A Triple-Mode Midinfrared Modulator for Radiative Heat Management of Objects with Various Emissivity

Haoming Fang, Wanrong Xie, Xiuqiang Li, Kebin Fan, Yi-Ting Lai, Bowen Sun, Shulin Bai, Willie J. Padilla, and Po-Chun Hsu*

Cite This: *Nano Lett.* 2021, 21, 4106–4114

Read Online

ACCESS | Metrics & More | Article Recommendations | Supporting Information

ABSTRACT: Thermal management is ubiquitous in the modern world and indispensable for a sustainable future. Radiative heat management provides unique advantages because the heat transfer can be controlled by the surface. However, different object emissivities require different tuning strategies, which poses challenges to develop dynamic and universal radiative heat management devices. Here, we demonstrate a triple-mode midinfrared modulator that can switch between passive heating and cooling suitable for all types of object surface emissivities. The device comprises a surface-textured infrared-semiabsorbing elastomer coated with a metallic back reflector, which is biaxially strained to sequentially achieve three fundamental modes: emission, reflection, and transmission. By analyzing and optimizing the coupling between optical and mechanical properties, we achieve a performance as follows: emittance contrast $\Delta\varepsilon$ = 0.58, transmittance contrast $\Delta\tau$ = 0.49, and reflectance contrast $\Delta\rho$ = 0.39. The device can provide a new design paradigm of radiation heat regulation for wearable, robotics, and camouflage technologies.

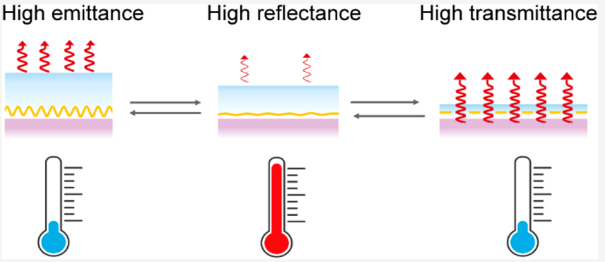

KEYWORDS: *thermal management, midinfrared modulator, dynamic tunability, radiative heat regulation, camouflage device*

Thermal management is widely used and critical in advanced technology.[1−3] For instance, batteries, solar cells, vehicles, and electronic chips all require careful thermal management to maintain suitable working temperature ranges.[4−10] On a larger scale, space heating and cooling maintain the indoor temperature all year round but also consume up to 20% of global energy.[11,12] Therefore, the development of more effective, energy-efficient, and universal thermal management technology is one of the most critical tasks for a sustainable future.[13−15]

Among all the thermal management mechanisms, radiation heat transfer is best known for its universality, media-free operation, and large tunability.[16,17] Materials with exotic radiative heat transfer properties were developed through photonic design and fabrication,[18−20] and they have shown great promise as an energy-efficient or even energy-free approach to achieve thermal management.[21,22] Fundamentally, the radiative property of any material has three components: reflectance (ρ, including both specular and diffuse), transmittance (τ), and absorptance (α), which add up to unity, i.e., $\rho + \tau + \alpha = 1$. According to Kirchhoff's law, at thermodynamic equilibrium, the absorptance equals the emittance (ε), $\alpha = \varepsilon$. Therefore, for radiatively opaque ($\tau = 0$) materials, $\alpha = \varepsilon = 1 - \rho$, and the total power ($P$) radiated from an object is given by Stefan−Boltzmann law: $P = A\varepsilon\sigma T^4$, where A is the surface area, σ is the Stefan−Boltzmann constant, and T is the object surface temperature. As shown in Figure 1A, to achieve radiative cooling for low-ε objects such as metals, the strategy is to apply a high-ε coating to promote thermal emission. For high-ε objects, such as the human body, the ideal cooling strategy is choose the device with high-τ materials allowing direct radiation from the skin surface. In contrast, the radiative heating strategy of applying low-ε opaque materials works for both low-ε and high-ε objects.[23] The dependence of cooling strategies on the object emissivity is further elaborated in Figure 1B,C. When a high-τ material is used for cooling, the heat transfer coefficient increases approximately linearly with the underlying object emissivity. For a high-ε material, the heat transfer coefficient depends only on the cooling material itself, but its thermal resistance prohibits it from achieving better cooling when the object emissivity is already high. Besides, the size of the air gap between object and film also plays an essential role in thermal transfer performance (detailed analysis of these hypothetical cooling materials and thermal circuit is shown in the Supporting Information). Taking the air gap of 1 mm as an example (Figure 1D), one can determine the high-ε-dominating and the high-τ-dominating regions for various

Received: March 21, 2021
Revised: April 20, 2021
Published: April 26, 2021

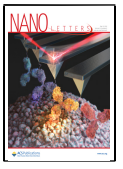

https://doi.org/10.1021/acs.nanolett.1c01147
Nano Lett. 2021, 21, 4106–4114

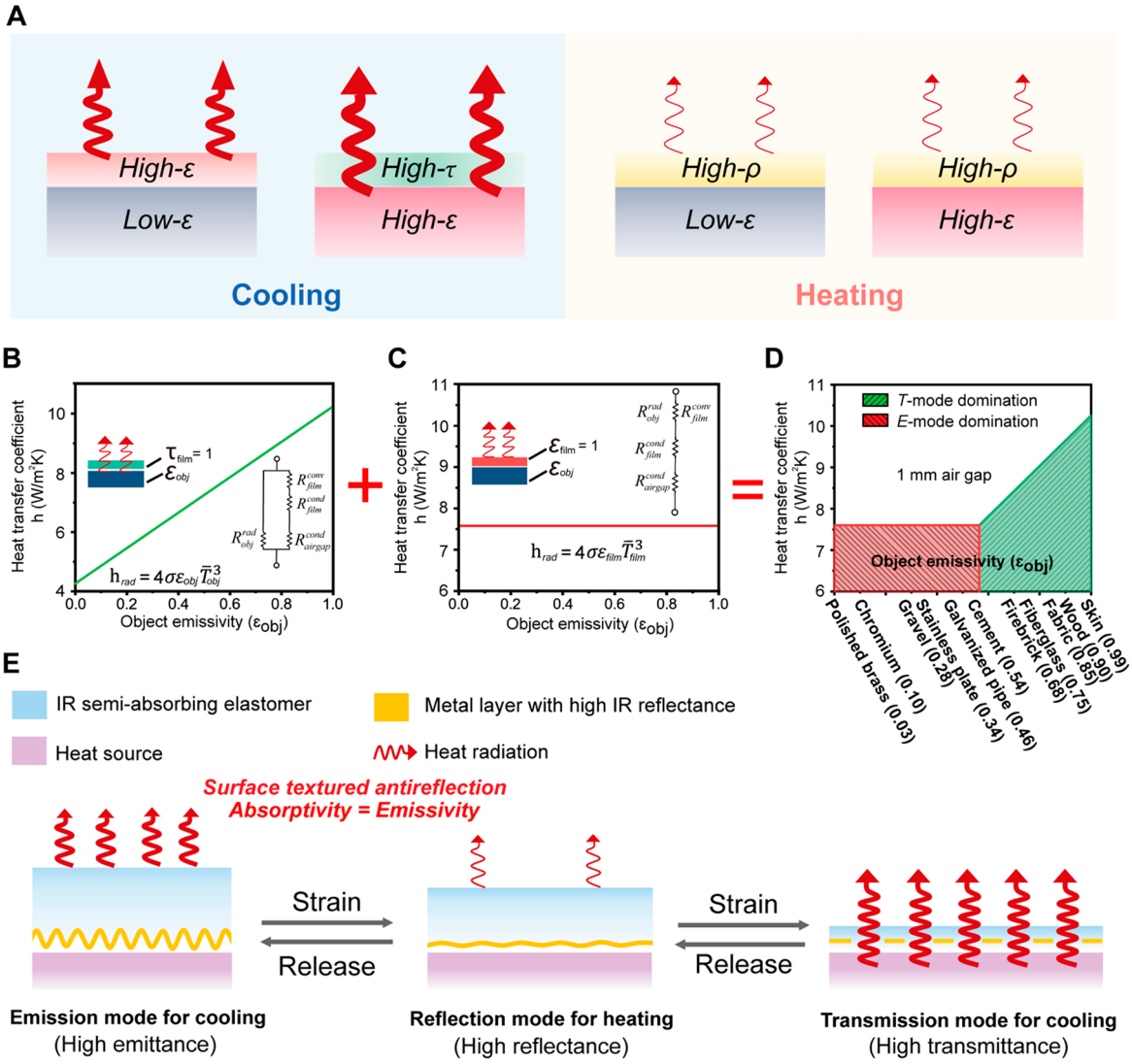

Figure 1. Design principle of the triple-mode mid-IR modulator for all-surface thermal management. (A) The best strategies for cooling high-emissive (high-ε) and low-emissive (low-ε) objects are by high-transmittance (high-τ) and high-emittance (high-ε) materials, respectively. For heating, using high reflectivity (high-ρ) material works for all objects. (B) When the radiative cooling strategy is by IR transmittance, the radiative heat transfer coefficient is dependent on the object's emissivity, which is less effective for low-emissivity objects. (C) When the radiative cooling strategy is by IR emittance, the radiative heat transfer coefficient is constant. (D) To achieve optimal radiative cooling on all kinds of object emissivities, the thermal-managing material must be able to switch between high transmittance and high emittance. (E) On the basis of optical and mechanical design, the thin-film mid-IR modulator can change among "emission-mode", "reflection-mode", and "transmission-mode" via mechanical actuation.

object emissivities. This result unambiguously shows the demand for the dynamic regulation among all three modes (emission, reflection, and transmission) is necessary to achieve universal radiative thermal management for an object with arbitrary emissivity.[24]

Here, we demonstrate a triple-mode polymer/metal elastomeric modulator that can dynamically switch among emission (E-mode), reflection (R-mode), and transmission (T-mode) to accomplish the management of the all-surface passive radiative cooling and heating. As shown in Figure 1E, in E-mode, the infrared (IR)-semiabsorbing elastomer is at zero strain and the largest thickness for absorption. The underlying metal layer has the highest roughness to promote diffuse scattering and further increases the absorption.[25] In R-mode, the film is biaxially stretched, which smooths the metal reflector and shrinks the elastomer thickness for high reflection. In T-mode, the film is stretched further to reduce the thickness and create voids on the metal film that results in high transmittance.

The realization of the triple-mode modulator calls for a rational design of both the mechanical properties and the optical structure.[26−31] For the elastomeric superstrate, the styrene−ethylene−butylene−styrene (SEBS) block copolymer is chosen because of its excellent mechanical properties, thickness-sensitive mid-IR absorption, and solution processability. The different polymer chain composition of SEBS results in different mid-IR absorption and mechanical properties. SEBS elastomers with higher polystyrene content have larger intrinsic absorption coefficient (μ_p) from the benzene ring, and they also have higher elastic modulus attributed from the physical cross-links of styrene groups (Figure S3). To reduce the actuation energy for elastic modulation and intermediate mid-IR absorption, SEBS with polystyrene content of 18.5−22.5% was chosen. In contrast, polyethylene

https://doi.org/10.1021/acs.nanolett.1c01147
Nano Lett. 2021, 21, 4106−4114

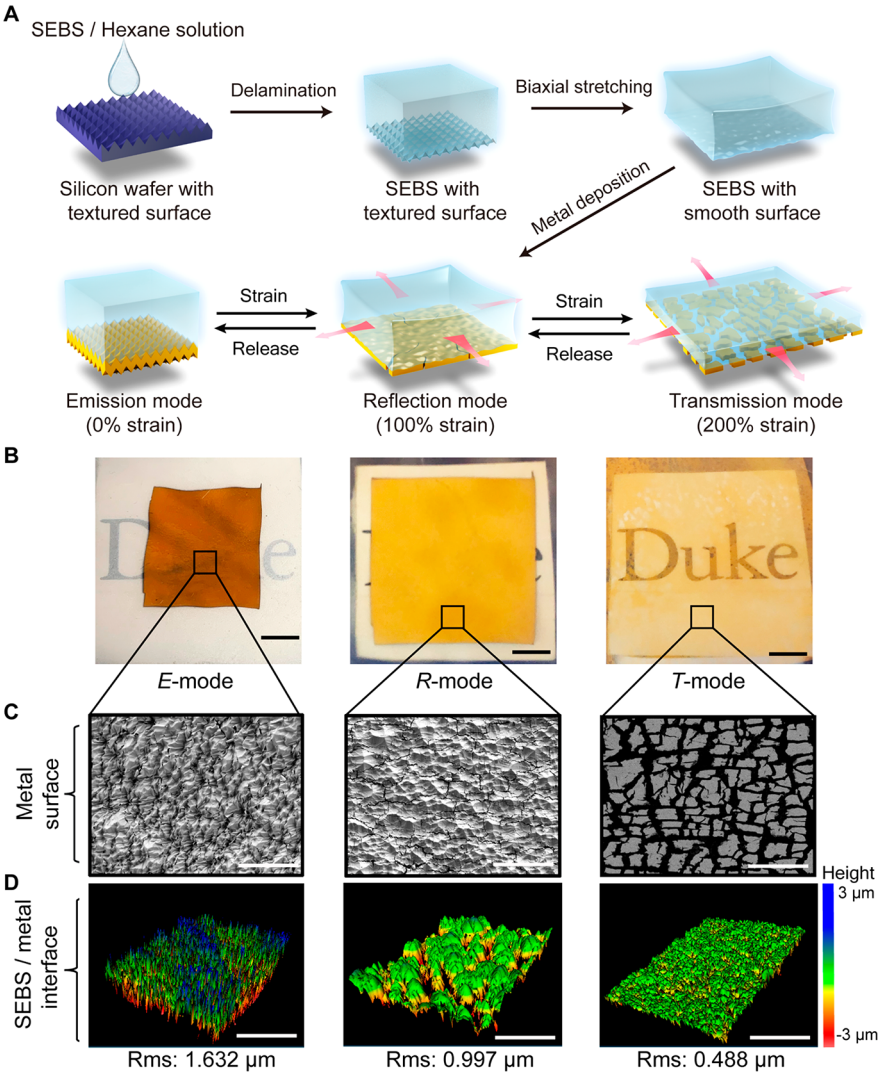

Figure 2. Fabrication and morphology characterization of the triple-mode modulator. (A) Schematic of film preparation method and the mechanical actuation of the triple-mode modulator with biaxial strains of 0% (left), 100% (middle), and 200% (right). (B) Digital camera images of the film under the biaxial strains of 0% (left), 100% (middle) and 200% (right). The scale bars are 5 mm. (Logo credit: Duke University). (C) SEM images from the metal side under the biaxial strains of 0% (left), 100% (middle), and 200% (right). The scale bars are 50 μm. (D) The 3D topographical maps from the SEBS side under the biaxial strains of 0% (left), 100% (middle), and 200% (right). The scale bars are 50 μm.

(PE) is IR-transparent but nonelastic, and polydimethylsiloxane (PDMS) elastomer is IR-opaque (Figure S4). Figure 2A illustrates the fabrication procedure. First, a 5 wt % SEBS/hexane solution is drop-cast onto a surface-textured silicon wafer to create a highly diffuse surface (Figure S6). This surface texturing plays an essential role for large IR emittance tunability, which will be elaborated in the next paragraph. The SEBS film was then delaminated from the wafer and biaxially stretched to 100% strain, followed by a deposition of 70 nm thick Ti/Au as the IR-reflective layer. At this tensile strain state, the film works in R-mode because the metal layer is at its lowest roughness state. After releasing the strain, the SEBS thickness increases, and the metal layer returns to the highly textured state, shifting the film to E-mode. When the film is stretched to 200% strain, the metal layer becomes islandlike and operates in T-mode. The three modes are characterized by a normal digital camera, SEM (from the metal side), and by an optical profiler (from the SEBS/metal interface), as shown in Figure 2B–D, respectively. In E-mode, the dark appearance is due to the antireflecting surface texture with an RMS roughness of 1.632 μm. When it is adjusted to R-mode, it becomes visually reflective, and the roughness decreases to 0.997 μm, showing the metal layer is smoothed. Further stretching of the film shifts it to T-mode, at which point it becomes visually transparent because the metal domains are separated from each other.

We attribute the emittance of the SEBS/metal film to both the SEBS thickness and the metal diffuse scattering[32,33] (Figure 3A) and perform a detailed analysis to maximize the emittance contrast. We define the total effective absorption coefficient (μ) to be the product of the intrinsic absorption coefficient (μ_p) and the enhancement factor (β) which is attributed to the increased optical path length compared with the planar back reflector. The transmittance of a smooth SEBS film without the metal back reflector is described by the Beer–Lambert law as $\tau = (1 - R)^2 \exp(-\mu L) = (1 - R)^2 \exp(\mu_p{}^d)$ where l is the light path length, d is the nominal film thickness, and R is the Fresnel reflection at the interface. By measuring the transmittance of smooth SEBS films without the metal back reflector (Figure S7), we determined $\mu_p = 0.00377\ \mu m^{-1}$

https://doi.org/10.1021/acs.nanolett.1c01147
Nano Lett. 2021, 21, 4106–4114

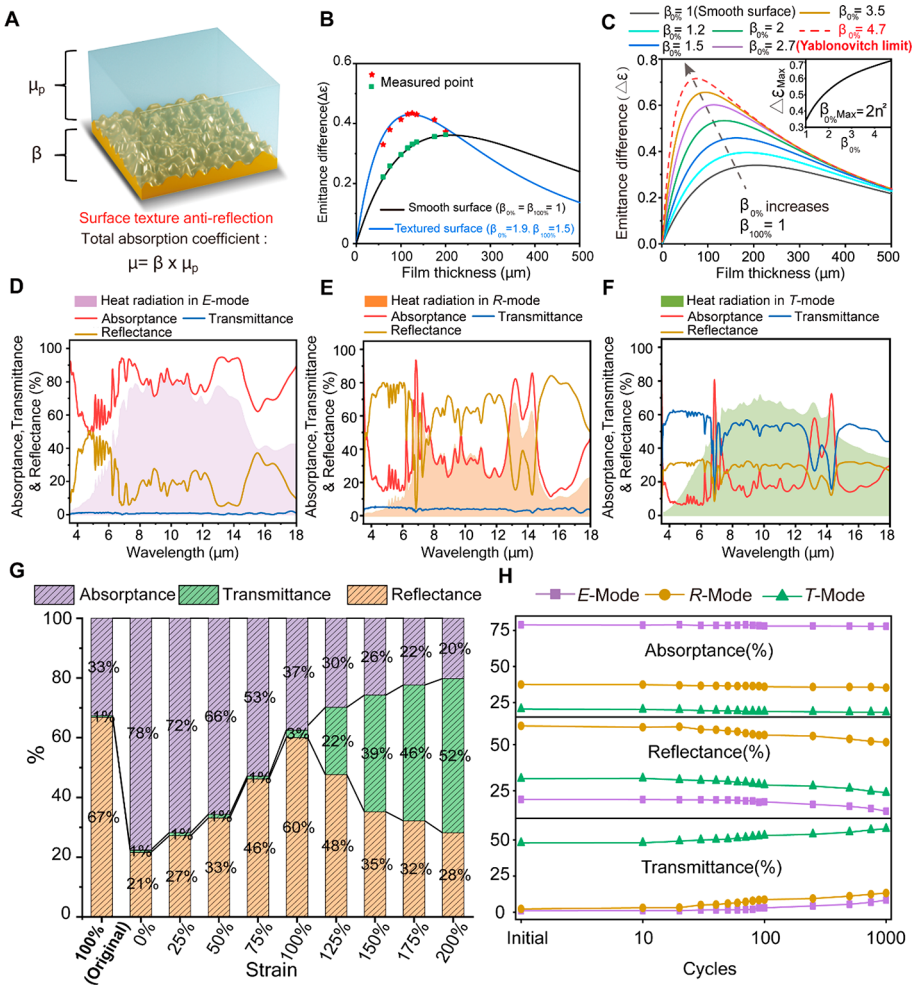

Figure 3. Infrared properties and strain-emittance coupled optimization. (A) Schematic of the sample model which consists of total absorption coefficient μ, intrinsic absorption coefficient μ_p and enhancement factor β. (B) Emittance difference between E- and R-mode in smooth (black line) and textured (blue line) SEBS film as a function of film thickness. The red stars and green squares represent the measured values. (C) Emittance difference with increasing $\beta_{0\%}$ and fixed $\beta_{100\%}$ = 1 as the function of film thickness. The inserted plot is the maximum emittance difference at different $\beta_{0\%}$. (D−F) Absorptance, transmittance, and reflectance of the triple-mode modulator with the strain of 0% (E-mode), 100% (R-mode), and 200% (T-mode) in the IR spectra from 3.5 to 18 μm. The shaded areas represent the resultant heat radiation. (G) Weighted-average absorptance, transmittance, and reflectance of the film under the biaxial strain from original 100% to 0% and then stepwise to 200%. (H) Cycle stability over 1000 cycle test of the weighted-average absorptance, transmittance, and reflectance of E-, R-, and T-mode.

(weighted-averaged over room temperature blackbody radiation spectra from 8 to 12 μm). Next, the β values are determined by measuring the reflectance ρ of SEBS/Au thin films of different strains, thicknesses, and surface morphologies. As shown in Figure 3B, the black curve represents the sample without surface texturing ($\beta_{0\%} = \beta_{100\%} = 1$), and the maximum emittance difference ($\Delta\varepsilon_{max}$) is 0.36 when the film thickness is approximately 200 μm at zero strain. When the inverse-pyramid texture is introduced to the SEBS film, $\Delta\varepsilon_{max}$ increases to 0.43 at a thickness of 125 μm, which corresponds to the enhancement factor $\beta_{0\%}$ at 0% strain and $\beta_{100\%}$ at 100% biaxial tensile strain. This semiempirical analysis provides the guideline for the materials design for superior tunability. It is also worth noting that biaxial stretching actuation performs better than the simple uniaxial and side-constrained uniaxial stretching methods (Supporting Information).

Apparently, $\Delta\varepsilon$ will further increase with a larger diffuse scattering contrast between two states. In Figure 3C, assuming $\beta_{0\%}$ = 1, as $\beta_{100\%}$ increases, $\Delta\varepsilon_{max}$ increases, and its corresponding thickness decreases. The theoretical upper limit of $\beta_{0\%}$ (and therefore the limit of $\beta_{0\%} - \beta_{100\%}$ and $\Delta\varepsilon$) occurs for a perfect Lambertian surface known as the Yablonovitch limit. On the basis of our definition of β, this upper limit dictates $\beta \leq 2n^2$, where n is the reflective index of the IR absorber. Inserting n_{SEBS} =1.56 yields $\Delta\varepsilon_{max}$ as high as 0.72 when $\beta_{0\%}$ = 4.7 and $\beta_{100\%}$ = 1, suggesting the promising modulation range between E-mode and R-mode via better optical structure design and engineering.[34,35]

It should be noted that the elastic-strain-induced light modulation has been extensively studied with promising functionalities and performances.[36] To the best of our knowledge, most prior reports focused on the wavelength regions of visible and near-IR (except for refs 27, 30, and 37), which have drastically different material property requirements from mid-IR regime. While we received inspiration from these works, our mid-IR triple modulator is the outcome of several new critical designs. First, we choose SEBS over PDMS because SEBS has the proper mid-IR absorption coefficient, and PDMS is too absorbing to be mechanically tunable with a proper thickness. Second, the additional surface texturing

https://doi.org/10.1021/acs.nanolett.1c01147
Nano Lett. 2021, 21, 4106−4114

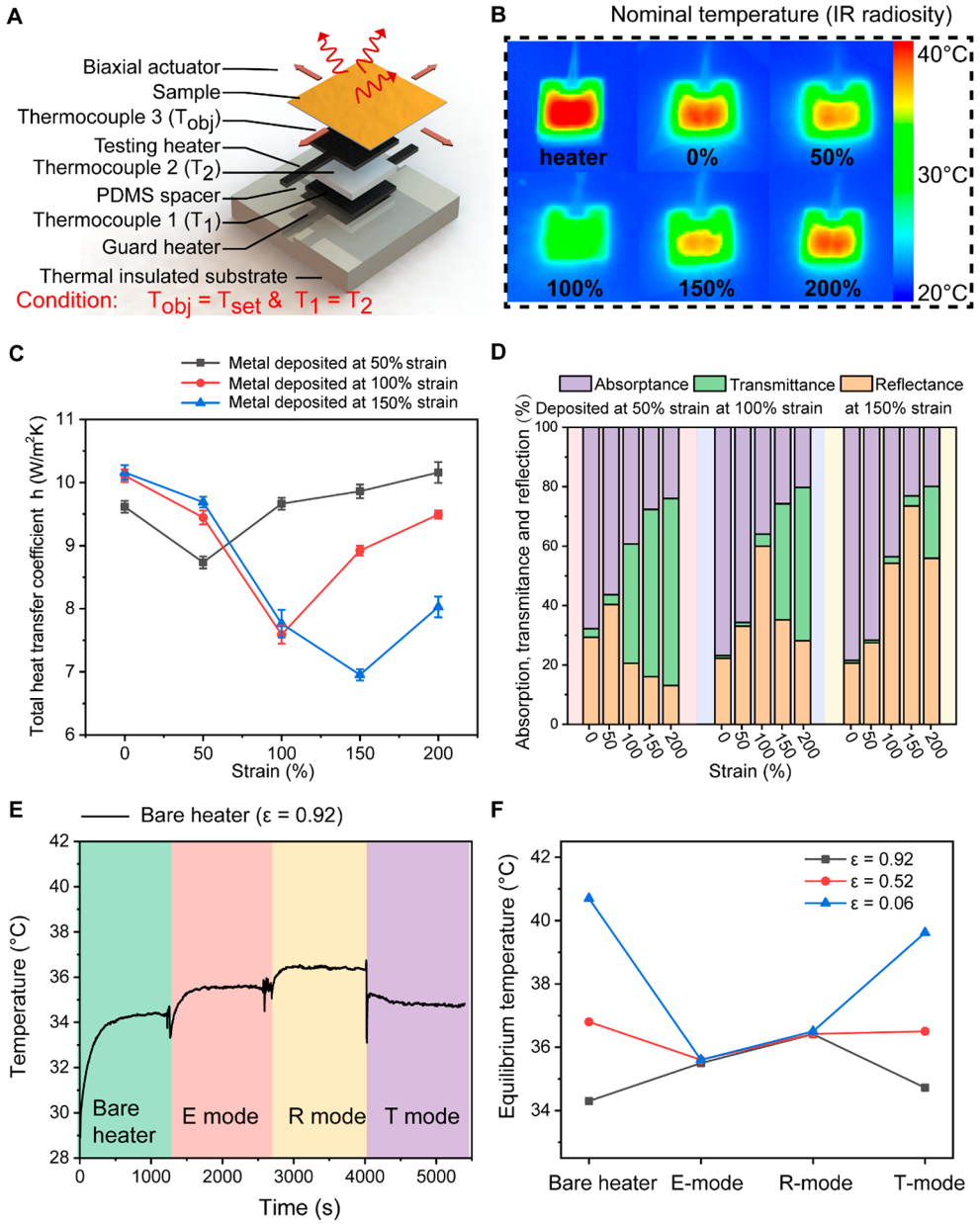

Figure 4. Thermal measurement of the triple-mode film. (A) Side view of steady-state measurement apparatus. (B) Top surface IR images of testing heater and sample under 0, 50, 100, 150, and 200% biaxial strain. (C) Total heat transfer coefficient of the film with metal deposited under 50% (dark gray line), 100% (red line), and 150% (blue line) biaxial strain as a function of strain. (D) Corresponding weighted-average absorptance, transmittance, and reflectance of the films with metal deposited under 50, 100, and 150% biaxial strain. (E) Actual temperature change among E-, R-, and T-modes (SEBS/metal film with metal deposited under 50% biaxial strain). (F) Equilibrium temperature at different states for heaters with different emissivity. Heater emissivity: black line, 0.92; red line, 0.52; and blue line, 0.06.

proved an essential factor for large emissivity tuning, which is in contrast with the interfacial wrinkling due to moduli mismatch. In Figure 3B, the SEBS/Au sample without surface texturing (marked as green squares) follows the smooth surface model with an emissivity contrast of only 0.31. This implies that without the additional surface texturing the strain-induced wrinkles do not have enough roughness to produce mid-IR diffuse scattering, and the emissivity contrast is caused solely by the thickness change. These two designs are the key factors for high modulation performance and are distinct from the visible/near-IR modulation.

In E-mode (Figure 3D), the modulator has the highest absorptance (emittance) of 78 ± 1% and a low transmittance of ~1%, owing to the corrugated metal as well as the largest SEBS thickness. In R-mode (Figure 3E), the reflectance dominates with a value of 60 ± 1%, and the transmittance becomes ~3 ± 1%. The slight increase in transmittance is caused by the voids between the metal plates. In T-mode (Figure 3F), the transmittance of the film rises to 52 ± 2%, while the reflectance and absorptance decrease to 28 ± 2% and 20 ± 1%, due to the isolated metal islands and the reduced SEBS thickness. The strong absorption peaks at the wavelengths of 6.3, 6.8, 7.2, 9.7, and 13.3 μm are attributed to the functional groups of SEBS such as −C═C−, $-CH_2-$, and ═C−H.[38] The shaded regions in each mode are the approximate heat radiation, suggesting the correlation between mid-IR modulation and radiative heat management. Figure 3G shows these three mid-IR properties after weighted-averaging over

https://doi.org/10.1021/acs.nanolett.1c01147
Nano Lett. 2021, 21, 4106−4114

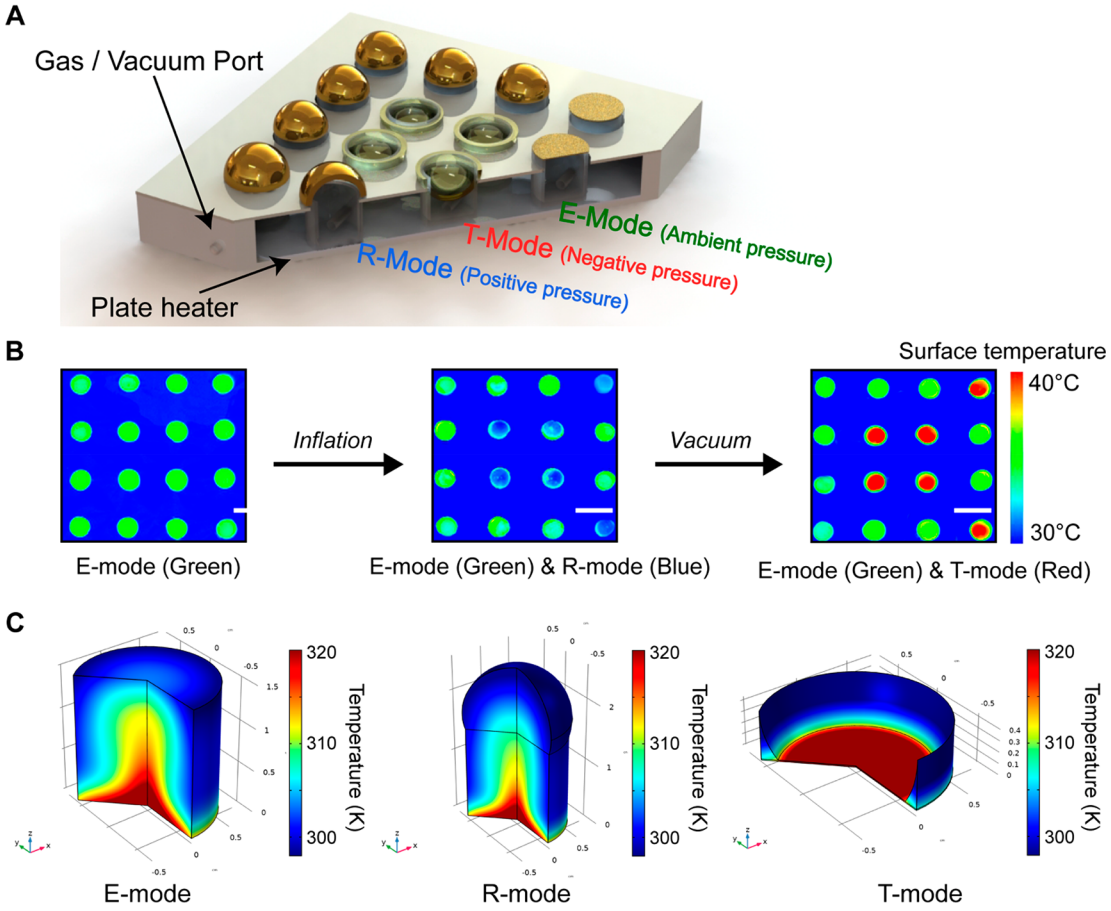

Figure 5. Pneumatic modulation of the IR appearance for 4 × 4 pixels device. (A) Schematic of the pneumatic device with a 4 × 4 pixels. E-mode is at ambient pressure. R-mode is at positive pressure, and T-mode is at negative pressure. (B) Top view IR image. Green dots, E-mode; blue dots, R-mode; and red dots, T-mode. The scale bars are 2 cm. (C) Temperature distribution of pixels in E-mode (left), R-mode (middle), and T-mode (right).

blackbody radiation when the strain varies from 0 to 200%. On moving from E-mode to R-mode, the reflectance increases by 39% with the same amount of emittance decrease. On shifting from R-mode to T-mode, the transmittance dominates the thermoregulatory performance by a 49% increase, and both reflectance and emittance decrease. Figure 3H shows the modulation is stable after 1000 strain cycles with around 10% change, indicating good cycle stability and reversibility when comparing with the reference in Table S9. The corresponding reflectance spectra including specular and diffuse reflectance among three modes are shown in Figure S21. Finally, it should be noted that the visible appearance and spectra (Figures 2B and S23) can be maintained and controlled independently from the mid-IR modulation. For example, creating submicrometer pores[39,40] in our SEBS film can act as strong Mie scatterers for visible light but weak Rayleigh scatterers for mid-IR light, thereby overriding the color change without affecting the mid-IR property.

The radiative heat management of the triple-mode modulator was validated by the apparatus as shown in Figures 4A and S30. Qualitatively, the IR images (Figure 4B) show the IR radiosity modulation under different strains. In Figure 4C, the total heat transfer coefficients of the triple-mode modulator are measured quantitively. The red line corresponds to the sample with 100% strain as the R-mode, and the heat transfer coefficients are 10.11 ± 0.11, 7.59 ± 0.14, and 9.49 ± 0.07 W/m^2 K for E-mode, R-mode, and T-mode, respectively. The heat transfer modulation range can be further controlled by depositing the metal back reflector at different strains (50% strain as dark gray and 150% strain as blue lines). The weighted-average mid-IR properties of these three samples are also measured and shown in Figure 4D. This demonstrates the versatility for designing and customizing the triple-mode radiative heat management device to suit various kinds of scenarios and environment requirements.[41,42] To further demonstrate the heat management functionality, we measured the temperature change of objects (electric heater) with different emissivities (Figure 4E,F). Notably, if our device is used for indoor personal thermal management, then this range of temperature modulation can result in an energy savings of several tens of percentages.[43] In Figure 4F, the three heaters behave similarly in E-mode and R-mode but diverge in T-mode. That is, the high-emissivity object uses T-mode for cooling, but the low-emissivity object uses E-mode for cooling. This result experimentally proves the need to have three modes for all-surface radiative heat modulation.

In addition to heat management, a pneumatic thermal camouflage device with a 4 × 4 matrix is fabricated, as shown in Figures 5A and S34. By regulating the air pressure, the SEBS/metal film on each pixel can change among E-mode, R-mode, and T-mode, further displaying different IR appearances and the letter "D" in different colors (Figure 5B). We designed

https://doi.org/10.1021/acs.nanolett.1c01147
Nano Lett. 2021, 21, 4106−4114

our pneumatic camouflage device to take advantage of both radiative heat transfer and convection/conduction. The flat configuration is in E-mode. Under positive pressure, the film bulges into a dome-shaped cap and is stretched to R-mode. Both the large air gap and low surface emissivity result in low surface radiosity and disguise it as a "cold object". Under negative pressure, the film was depressed and stretched into T-mode, in which the narrow air gap and high transmittance maximize the radiosity and show up as a "hot object". This pneumatic soft actuation[44] enables rapid and highly reversible thermal radiation control and combines both functions of IR camouflage and heat management. Among E-mode, R-mode, and T-mode, the apparent temperature contrast between pixels is approximately 5 °C. We further individually control the pressure of the pixels to show its capability as a thermal radiation display. To better predict the radiative response, COMSOL Multiphysics was used to simulate the temperature distribution inside the pixels (in Figure 5C) to calculate the radiosity among these three modes (in Table S7).

DISCUSSION

In summary, the triple-mode mid-IR modulator has demonstrated its capability to accomplish all-surface passive radiative cooling and heating management and mid-IR camouflage. It is the first experimental demonstration of a triple-mode mid-IR radiative-heat-managing device, together with numerical modeling as theoretical support. We experimentally proved the dependence of radiative heat management on the object's emissivity, thus it is necessary to combine three modes on the same device to achieve multifunctionality. The mechanism study of emissivity−strain correlation among tunability, film thickness, and scattering roughness also serves as a useful guideline for the research community for further development.

Besides mechanical actuation, we envision the triple-mode mid-IR modulation concept can also be accomplished by other methods such as thermochromic phase-transition-induced IR modulation,[45−47] electrochemical-induced modulation[48,49] of the IR reflectance, ultraviolet (UV)-light-induced modulation,[50] and liquid-induced modulation,[51,52] with different pros and cons and corresponding suitable applications (Table S8). It should be noted that different applications have various engineering constraints to overcome. This work's scope focuses on the in-depth study of the triple-mode radiative heat modulator in the mid-IR regime that is more suitable for indoor scenarios. Further expanding the modulation to visible and near-IR regimes and considering multimodal heat management would be rewarding. For IR camouflage, thermal metamaterials[53−57] with judiciously engineered thermal conductance show great promise by concealing the object without a priori knowledge of the background thermal radiation. It is anticipated that the incorporation of metasurface design and dynamic materials tuning can bring substantial synergistic benefits. With the proof-of-concept demonstration, many other exciting future works can be pursued with multidisciplinary efforts, such as plasmonic metamaterials, photonic crystals, device miniaturization, artificial intelligence-enabled camouflage, and integrated wearability. Overall, we envision this versatile and effective approach will endow immense opportunities for photonics, radiation heat transfer, robotics, and energy science.

ASSOCIATED CONTENT

Supporting Information

The Supporting Information is available free of charge at https://pubs.acs.org/doi/10.1021/acs.nanolett.1c01147.

Experimental procedures, heat transfer calculations, additional mechanical and mid-IR properties, SEM images, mechanical properties, UV−vis spectra, environmental stability test, performance comparison with literature, COMSOL modeling (PDF)

AUTHOR INFORMATION

Corresponding Author

Po-Chun Hsu − *Department of Mechanical Engineering and Materials Science, Duke University, Durham, North Carolina 27708, United States;* orcid.org/0000-0002-6509-9377; Email: pochun.hsu@duke.edu

Authors

Haoming Fang − *Department of Mechanical Engineering and Materials Science, Duke University, Durham, North Carolina 27708, United States; Department of Materials Science and Engineering, HEDPS/CAPT/LTCS, Key Laboratory of Polymer Chemistry and Physics of Ministry of Education, College of Engineering, Peking University, Beijing 100871, China*

Wanrong Xie − *Department of Mechanical Engineering and Materials Science, Duke University, Durham, North Carolina 27708, United States; College of Materials Science and Engineering, Beijing University of Chemical Technology, Beijing 100029, China*

Xiuqiang Li − *Department of Mechanical Engineering and Materials Science, Duke University, Durham, North Carolina 27708, United States;* orcid.org/0000-0002-5785-650X

Kebin Fan − *Department of Electrical and Computer Engineering, Duke University, Durham, North Carolina 27708, United States*

Yi-Ting Lai − *Department of Mechanical Engineering and Materials Science, Duke University, Durham, North Carolina 27708, United States*

Bowen Sun − *Department of Mechanical Engineering and Materials Science, Duke University, Durham, North Carolina 27708, United States*

Shulin Bai − *Department of Materials Science and Engineering, HEDPS/CAPT/LTCS, Key Laboratory of Polymer Chemistry and Physics of Ministry of Education, College of Engineering, Peking University, Beijing 100871, China;* orcid.org/0000-0001-9177-7525

Willie J. Padilla − *Department of Electrical and Computer Engineering, Duke University, Durham, North Carolina 27708, United States;* orcid.org/0000-0001-7734-8847

Complete contact information is available at: https://pubs.acs.org/10.1021/acs.nanolett.1c01147

Author Contributions

P.-C.H. and H.F. conceived the idea. H.F. and W.X. prepared the triple-mode samples. H.F and W.X designed and fabricated the biaxial actuator. H.F., B.S., and Y.-T.L. designed and conducted the thermal measurements. W.J.P., H.F., and K.F conducted the FTIR spectrometry measurement. H.F. and X.L tested and simulated mechanical properties. P.-C.H. supervised the project. S.B and W.J.P. assisted with the data

https://doi.org/10.1021/acs.nanolett.1c01147
Nano Lett. 2021, 21, 4106−4114

interpretation. All authors discussed the results and contributed to the writing of the paper.

Notes

The authors declare the following competing financial interest(s): P.-C.H. and H.F are listed as inventors on a provisional U.S. patent application from the Duke University, which describes the design and working mechanism of an all-surface radiative thermal managing device. The remaining authors declare no competing interests.

■ ACKNOWLEDGMENTS

The authors thank the Pratt School of Engineering at Duke University for the funding support and the Shared Materials Instrumentation Facility (SMIF) for its technical support. H.M.F also acknowledges the China Scholarship Council for their financial support.

■ REFERENCES

(1) DeRolph, C. R.; McManamay, R. A.; Morton, A. M.; Nair, S. S. City energysheds and renewable energy in the United States. *Nat. Sustain* **2019**, *2*, 412−420.
(2) Chu, S.; Majumdar, A. Opportunities and challenges for a sustainable energy future. *Nature* **2012**, *488*, 294−303.
(3) Bell, L. E. Cooling, Heating, Generating Power, and Recovering Waste Heat with Thermoelectric Systems. *Science* **2008**, *321*, 1457−1461.
(4) Rodrigues, M.-T. F.; Babu, G.; Gullapalli, H.; Kalaga, K.; Sayed, F. N.; Kato, K.; Joyner, J.; Ajayan, P. M. A materials perspective on Li-ion batteries at extreme temperatures. *Nat. Energy* **2017**, *2*, 17108.
(5) Hao, M.; Li, J.; Park, S.; Moura, S.; Dames, C. Efficient thermal management of Li-ion batteries with a passive interfacial thermal regulator based on a shape memory alloy. *Nat. Energy* **2018**, *3*, 899−906.
(6) Bierman, D. M.; Lenert, A.; Chan, W. R.; Bhatia, B.; Celanović, I.; Soljačić, M.; Wang, E. N. Enhanced photovoltaic energy conversion using thermally based spectral shaping. *Nat. Energy* **2016**, *1*, 16068.
(7) Li, W.; Shi, Y.; Chen, K.; Zhu, L.; Fan, S. A Comprehensive Photonic Approach for Solar Cell Cooling. *ACS Photonics* **2017**, *4*, 774−782.
(8) Kneissl, M.; Seong, T.-Y.; Han, J.; Amano, H. The emergence and prospects of deep-ultraviolet light-emitting diode technologies. *Nat. Photonics* **2019**, *13*, 233−244.
(9) Green, M. A.; Bremner, S. P. Energy conversion approaches and materials for high-efficiency photovoltaics. *Nat. Mater.* **2017**, *16*, 23−34.
(10) Padture, N. P. Advanced structural ceramics in aerospace propulsion. *Nat. Mater.* **2016**, *15*, 804−809.
(11) Booten, C., Robertson, J., Christensen, D., Heaney, M., Brown, D., Norton, P., Smith, C. *Residential Indoor Temperature Study*; Technical Report No. NREL/TP-5500-68019; National Renewable Energy Laboratory, 2017.
(12) Svetozarevic, B.; Begle, M.; Jayathissa, P.; Caranovic, S.; Shepherd, R. F.; Nagy, Z.; Hischier, I.; Hofer, J.; Schlueter, A. Dynamic photovoltaic building envelopes for adaptive energy and comfort management. *Nature Energy* **2019**, *4*, 671−682.
(13) Chu, S.; Cui, Y.; Liu, N. The path towards sustainable energy. *Nat. Mater.* **2017**, *16*, 16−22.
(14) Raman, A. P.; Anoma, M. A.; Zhu, L.; Rephaeli, E.; Fan, S. Passive radiative cooling below ambient air temperature under direct sunlight. *Nature* **2014**, *515*, 540−544.
(15) Li, T.; Zhai, Y.; He, S.; Gan, W.; Wei, Z.; Heidarinejad, M.; Dalgo, D.; Mi, R.; Zhao, X.; Song, J.; et al. A radiative cooling structural material. *Science* **2019**, *364*, 760−763.
(16) Fan, S. Thermal Photonics and Energy Applications. *Joule* **2017**, *1*, 264−273.
(17) Hsu, P.-C.; Liu, C.; Song, A. Y.; Zhang, Z.; Peng, Y.; Xie, J.; Liu, K.; Wu, C.-L.; Catrysse, P. B.; Cai, L.; et al. A dual-mode textile for human body radiative heating and cooling. *Sci. Adv.* **2017**, *3*, No. e1700895.
(18) De Zoysa, M.; Asano, T.; Mochizuki, K.; Oskooi, A.; Inoue, T.; Noda, S. Conversion of broadband to narrowband thermal emission through energy recycling. *Nat. Photonics* **2012**, *6*, 535−539.
(19) Baranov, D. G.; Xiao, Y.; Nechepurenko, I. A.; Krasnok, A.; Alù, A.; Kats, M. A. Nanophotonic engineering of far-field thermal emitters. *Nat. Mater.* **2019**, *18*, 920−930.
(20) Lozano, L. M.; Hong, S.; Huang, Y.; Zandavi, H.; El Aoud, Y. A.; Tsurimaki, Y.; Zhou, J.; Xu, Y.; Osgood, R. M.; Chen, G.; Boriskina, S. V. Optical engineering of polymer materials and composites for simultaneous color and thermal management. *Opt. Mater. Express* **2019**, *9*, 1990−2005.
(21) Mandal, J.; Fu, Y.; Overvig, A. C.; Jia, M.; Sun, K.; Shi, N. N.; Zhou, H.; Xiao, X.; Yu, N.; Yang, Y. Hierarchically porous polymer coatings for highly efficient passive daytime radiative cooling. *Science* **2018**, *362*, 315−319.
(22) Boriskina, S. V. Nanoporous fabrics could keep you cool. *Science* **2016**, *353*, 986−987.
(23) Cai, L.; Song, A. Y.; Wu, P.; Hsu, P.-C.; Peng, Y.; Chen, J.; Liu, C.; Catrysse, P. B.; Liu, Y.; Yang, A.; et al. Warming up human body by nanoporous metallized polyethylene textile. *Nat. Commun.* **2017**, *8*, 496.
(24) Qian, X.; Zhao, Y.; Alsaid, Y.; Wang, X.; Hua, M.; Galy, T.; Gopalakrishna, H.; Yang, Y.; Cui, J.; Liu, N.; et al. Artificial phototropism for omnidirectional tracking and harvesting of light. *Nat. Nanotechnol.* **2019**, *14*, 1048−1055.
(25) Han, S. E.; Chen, G. Toward the Lambertian Limit of Light Trapping in Thin Nanostructured Silicon Solar Cells. *Nano Lett.* **2010**, *10*, 4692−4696.
(26) Bai, R.; Suo, Z. Optomechanics of Soft Materials. *J. Appl. Mech.* **2015**, *82*, 071011.
(27) Xu, C.; Stiubianu, G. T.; Gorodetsky, A. A. Adaptive infrared-reflecting systems inspired by cephalopods. *Science* **2018**, *359*, 1495−1500.
(28) Kolle, M.; Lethbridge, A.; Kreysing, M.; Baumberg, J. J.; Aizenberg, J.; Vukusic, P. Bio-Inspired Band-Gap Tunable Elastic Optical Multilayer Fibers. *Adv. Mater.* **2013**, *25*, 2239−2245.
(29) Wang, Q.; Gossweiler, G. R.; Craig, S. L.; Zhao, X. Cephalopod-inspired design of electro-mechano-chemically responsive elastomers for on-demand fluorescent patterning. *Nat. Commun.* **2014**, *5*, 4899.
(30) Leung, E. M.; Colorado Escobar, M.; Stiubianu, G. T.; Jim, S. R.; Vyatskikh, A. L.; Feng, Z.; Garner, N.; Patel, P.; Naughton, K. L.; Follador, M.; et al. A dynamic thermoregulatory material inspired by squid skin. *Nat. Commun.* **2019**, *10*, 1947.
(31) Krishna, A.; Kim, J. M.; Leem, J.; Wang, M. C.; Nam, S.; Lee, J. Ultraviolet to Mid-Infrared Emissivity Control by Mechanically Reconfigurable Graphene. *Nano Lett.* **2019**, *19*, 5086−5092.
(32) Fei Guo, C.; Sun, T.; Cao, F.; Liu, Q.; Ren, Z. Metallic nanostructures for light trapping in energy-harvesting devices. *Light: Sci. Appl.* **2014**, *3*, No. e161.
(33) Yablonovitch, E. Statistical ray optics. *J. Opt. Soc. Am.* **1982**, *72*, 899.
(34) Wang, K. X.; Guo, Y.; Yu, Z. Light trapping in photonic structures. In *Semiconductors and Semimetals*; Elsevier, 2019; pp 45−91.
(35) Yu, Z.; Raman, A.; Fan, S. Fundamental limit of nanophotonic light trapping in solar cells. *Proc. Natl. Acad. Sci. U. S. A.* **2010**, *107*, 17491−17496.
(36) Zeng, S.; Zhang, D.; Huang, W.; Wang, Z.; Freire, S. G.; Yu, X.; Smith, A. T.; Huang, E. Y.; Nguon, H.; Sun, L. Bio-inspired sensitive and reversible mechanochromisms via strain-dependent cracks and folds. *Nat. Commun.* **2016**, *7*, 11802.
(37) Xu, C.; Colorado Escobar, M.; Gorodetsky, A. A. Stretchable Cephalopod-Inspired Multimodal Camouflage Systems. *Adv. Mater.* **2020**, *32*, 1905717.
(38) Zhou, T.; Zhang, A.; Zhao, C.; Liang, H.; Wu, Z.; Xia, J. Molecular Chain Movements and Transitions of SEBS above Room

https://doi.org/10.1021/acs.nanolett.1c01147
Nano Lett. 2021, 21, 4106−4114

Temperature Studied by Moving-Window Two-Dimensional Correlation Infrared Spectroscopy. *Macromolecules* **2007**, *40*, 9009−9017.
(39) Xu, Y.; Sun, B.; Ling, Y.; Fei, Q.; Chen, Z.; Li, X.; Guo, P.; Jeon, N.; Goswami, S.; Liao, Y.; et al. Multiscale porous elastomer substrates for multifunctional on-skin electronics with passive-cooling capabilities. *Proc. Natl. Acad. Sci. U. S. A.* **2020**, *117*, 205−213.
(40) Peng, Y.; Chen, J.; Song, A. Y.; Catrysse, P. B.; Hsu, P.-C.; Cai, L.; Liu, B.; Zhu, Y.; Zhou, G.; Wu, D. S.; et al. Nanoporous polyethylene microfibres for large-scale radiative cooling fabric. *Nat. Sustain* **2018**, *1*, 105−112.
(41) Lim, X. The super-cool materials that send heat to space. *Nature* **2020**, *577*, 18−20.
(42) Zhang, X. A.; Yu, S.; Xu, B.; Li, M.; Peng, Z.; Wang, Y.; Deng, S.; Wu, X.; Wu, Z.; Ouyang, M.; et al. Dynamic gating of infrared radiation in a textile. *Science* **2019**, *363*, 619−623.
(43) Hsu, P.-C.; Song, A. Y.; Catrysse, P. B.; Liu, C.; Peng, Y.; Xie, J.; Fan, S.; Cui, Y. Radiative human body cooling by nanoporous polyethylene textile. *Science* **2016**, *353*, 1019−1023.
(44) Yang, D.; Mosadegh, B.; Ainla, A.; Lee, B.; Khashai, F.; Suo, Z.; Bertoldi, K.; Whitesides, G. M. Buckling of Elastomeric Beams Enables Actuation of Soft Machines. *Adv. Mater.* **2015**, *27*, 6323−6327.
(45) Xiao, L.; Ma, H.; Liu, J.; Zhao, W.; Jia, Y.; Zhao, Q.; Liu, K.; Wu, Y.; Wei, Y.; Fan, S.; et al. Fast Adaptive Thermal Camouflage Based on Flexible VO_2/Graphene/CNT Thin Films. *Nano Lett.* **2015**, *15*, 8365−8370.
(46) Du, K.-K.; Li, Q.; Lyu, Y.-B.; Ding, J.-C.; Lu, Y.; Cheng, Z.-Y.; Qiu, M. Control over emissivity of zero-static-power thermal emitters based on phase-changing material GST. *Light: Sci. Appl.* **2017**, *6*, No. e16194.
(47) Li, X.-H.; Liu, C.; Feng, S.-P.; Fang, N. X. Broadband Light Management with Thermochromic Hydrogel Microparticles for Smart Windows. *Joule* **2019**, *3*, 290−302.
(48) Li, M.; Liu, D.; Cheng, H.; Peng, L.; Zu, M. Manipulating metals for adaptive thermal camouflage. *Science Advances* **2020**, *6*, No. eaba3494.
(49) Mandal, J.; Du, S.; Dontigny, M.; Zaghib, K.; Yu, N.; Yang, Y. Li4Ti5O12: A Visible-to-Infrared Broadband Electrochromic Material for Optical and Thermal Management. *Adv. Funct. Mater.* **2018**, *28*, 1802180.
(50) Coppens, Z. J.; Valentine, J. G. Spatial and Temporal Modulation of Thermal Emission. *Adv. Mater.* **2017**, *29*, 1701275.
(51) Mandal, J.; Jia, M.; Overvig, A.; Fu, Y.; Che, E.; Yu, N.; Yang, Y. Porous Polymers with Switchable Optical Transmittance for Optical and Thermal Regulation. *Joule* **2019**, *3*, 3088−3099.
(52) Morin, S. A.; Shepherd, R. F.; Kwok, S. W.; Stokes, A. A.; Nemiroski, A.; Whitesides, G. M. Camouflage and Display for Soft Machines. *Science* **2012**, *337*, 828−832.
(53) Peng, Y.; Li, Y.; Cao, P.; Zhu, X.; Qiu, C. 3D Printed Meta-Helmet for Wide-Angle Thermal Camouflages. *Adv. Funct. Mater.* **2020**, *30*, 2002061.
(54) Li, Y.; Bai, X.; Yang, T.; Luo, H.; Qiu, C.-W. Structured thermal surface for radiative camouflage. *Nat. Commun.* **2018**, *9*, 273.
(55) Yang, T.; Bai, X.; Gao, D.; Wu, L.; Li, B.; Thong, J. T. L.; Qiu, C. Invisible Sensors: Simultaneous Sensing and Camouflaging in Multiphysical Fields. *Adv. Mater.* **2015**, *27*, 7752−7758.
(56) Li, Y.; Zhu, K.-J.; Peng, Y.-G.; Li, W.; Yang, T.; Xu, H.-X.; Chen, H.; Zhu, X.-F.; Fan, S.; Qiu, C.-W. Thermal meta-device in analogue of zero-index photonics. *Nat. Mater.* **2019**, *18*, 48−54.
(57) Hu, R.; Huang, S.; Wang, M.; Luo, X.; Shiomi, J.; Qiu, C. Encrypted Thermal Printing with Regionalization Transformation. *Adv. Mater.* **2019**, *31*, 1807849.

https://doi.org/10.1021/acs.nanolett.1c01147
Nano Lett. 2021, 21, 4106−4114